Sickle cell anemia mice develop a unique cardiomyopathy with restrictive physiology

Nihal Bakeer[a,b,c], Jeanne James[d,e], Swarnava Roy[b,c], Janaka Wansapura[f,g], Shiva Kumar Shanmukhappa[h], John N. Lorenz[i], Hanna Osinska[e,j], Kurt Backer[b,c], Anne-Cecile Huby[d,e,j], Archana Shrestha[b,c], Omar Niss[a,c], Robert Fleck[k], Charles T. Quinn[a,c], Michael D. Taylor[d,e,j], Enkhsaikhan Purevjav[e,j], Bruce J. Aronow[l], Jeffrey A. Towbin[d,e,j], and Punam Malik[a,b,c,1]

[a]Division of Hematology, Cincinnati Children's Hospital Medical Center, Cincinnati, OH 45229; [b]Division of Experimental Hematology and Cancer Biology, Cincinnati Children's Hospital Medical Center, Cincinnati, OH 45229; [c]Cancer and Blood Diseases Institute, Cincinnati Children's Hospital Medical Center, Cincinnati, OH 45229; [d]Division of Cardiology, Cincinnati Children's Hospital Medical Center, Cincinnati, OH 45229; [e]Heart Institute, Cincinnati Children's Hospital Medical Center, Cincinnati, OH 45229; [f]Imaging Research Center, Cincinnati Children's Hospital Medical Center, Cincinnati, OH 45229; [g]Department of Physics, University of Colombo, Colombo 03, Sri Lanka; [h]Department of Pathology, Cincinnati Children's Hospital Medical Center, Cincinnati, OH 45229; [i]Department of Molecular and Cellular Physiology, University of Cincinnati, Cincinnati, OH 45267; [j]Division of Molecular Cardiovascular Biology, Cincinnati Children's Hospital Medical Center, Cincinnati, OH 45229; [k]Department of Radiology, Cincinnati Children's Hospital Medical Center, Cincinnati, OH 45229; and [l]Division of Biomedical Informatics, Cincinnati Children's Hospital Medical Center, Cincinnati, OH 45229

Edited by J. G. Seidman, Harvard Medical School, Boston, MA, and approved June 24, 2016 (received for review January 7, 2016)

Cardiopulmonary complications are the leading cause of mortality in sickle cell anemia (SCA). Elevated tricuspid regurgitant jet velocity, pulmonary hypertension, diastolic, and autonomic dysfunction have all been described, but a unifying pathophysiology and mechanism explaining the poor prognosis and propensity to sudden death has been elusive. Herein, SCA mice underwent a longitudinal comprehensive cardiac analysis, combining state-of-the-art cardiac imaging with electrocardiography, histopathology, and molecular analysis to determine the basis of cardiac dysfunction. We show that in SCA mice, anemia-induced hyperdynamic physiology was gradually superimposed with restrictive physiology, characterized by progressive left atrial enlargement and diastolic dysfunction with preserved systolic function. This phenomenon was absent in WT mice with experimentally induced chronic anemia of similar degree and duration. Restrictive physiology was associated with microscopic cardiomyocyte loss and secondary fibrosis detectable as increased extracellular volume by cardiac-MRI. Ultrastructural mitochondrial changes were consistent with severe chronic hypoxia/ischemia and sarcomere diastolic-length was shortened. Transcriptome analysis revealed up-regulation of genes involving angiogenesis, extracellular-matrix, circadian-rhythm, oxidative stress, and hypoxia, whereas ion-channel transport and cardiac conduction were down-regulated. Indeed, progressive corrected QT prolongation, arrhythmias, and ischemic changes were noted in SCA mice before sudden death. Sudden cardiac death is common in humans with restrictive cardiomyopathies and long QT syndromes. Our findings may thus provide a unifying cardiac pathophysiology that explains the reported cardiac abnormalities and sudden death seen in humans with SCA.

sickle cell anemia | cardiomyopathy | restrictive physiology | arrhythmias | sudden death

Sickle cell anemia (SCA) results from a point mutation in the β-globin gene and affects millions world-wide. It is characterized by production of the mutant hemoglobin S (HbS), which polymerizes upon deoxygenation and distorts the shape of RBCs, increasing their propensity to hemolysis and microvascular occlusion. Recurrent cycles of HbS polymerization result in a host of acute and chronic complications, including vaso-occlusive pain crisis, chronic hemolytic anemia, and organ damage. SCA-associated mortality rates have improved because of early diagnosis with universal newborn screening, immunization, and penicillin prophylaxis, which has changed the natural history of SCA (1, 2) and the impact of SCA on organ pathologies is now becoming evident.

Despite improved early survival, nearly one-third of young adults with SCA die suddenly (3–9). The sickle myocardium has been presumed to be relatively resistant to the effects of sickling (10), and studies/autopsies show little evidence of atherosclerosis or coronary disease (11–14). Mildly increased systolic pulmonary arterial pressure (PAP) estimated by tricuspid regurgitant jet velocity (TRV) of >2.5 m/s by echocardiography has been shown to be an independent risk factor for early mortality (odds ratio 8–15) (5, 15–20). This finding was initially considered to be consistent with pulmonary arterial hypertension (PH) (5, 17, 21–25). However, right heart catheterization studies show that only 25–30% of patients with TRV ≥ 2.5 m/s truly have PH, with the majority having pulmonary venous hypertension (18, 26–29). Indeed, PAP in SCA patients was only modestly elevated to 30–60 mmHg (30), in contrast to patients with idiopathic PH. Increased left ventricular (LV) mass and chamber sizes in the setting of normal systolic function are well-known findings in SCA (31–35) and have been attributed to a high-output state from the chronic anemia (31, 36). More recently, evidence of diastolic dysfunction has emerged in patients with SCA (37–40), the mechanism of which remains unknown. Unlike the iron overload-related diastolic dysfunction seen in patients with β-thalassemia (41), myocardial iron deposition is not seen in patients with SCA with diastolic dysfunction

Significance

Sickle cell anemia (SCA) is a common monogenic disorder associated with significant morbidity and mortality and a high incidence of unexplained sudden death in young adults. With the prevention of infections, there is an increasing appreciation for cardiopulmonary complications and a cardiac phenotype that cannot be solely attributed to chronic anemia. We used mouse models of SCA and iron-deficient anemia to show distinct functional, pathological, ultrastructural, and molecular cardiac features causing a unique restrictive cardiomyopathy in SCA that predisposed the myocardium to electrophysiological abnormalities and sudden death. This is a comprehensive longitudinal analysis in preclinical mouse models that unifies the previously reported diverse cardiac phenotypes in SCA, and opens new avenues for early diagnostics and targeted therapies for human SCA-related cardiac disease.

Author contributions: P.M. designed research; N.B., J.J., S.R., J.W., S.K.S., J.N.L., H.O., K.B., A.-C.H., and A.S. performed research; N.B., J.J., S.R., J.W., S.K.S., J.N.L., H.O., A.-C.H., O.N., R.F., C.T.Q., M.D.T., E.P., B.J.A., J.A.T., and P.M. analyzed data; N.B., J.J., and P.M. wrote the paper; and J.A.T. and P.M. conceived the project.

The authors declare no conflict of interest.

This article is a PNAS Direct Submission.

Freely available online through the PNAS open access option.

See Commentary on page 9670.

[1]To whom correspondence should be addressed. Email: punam.malik@cchmc.org.

This article contains supporting information online at www.pnas.org/lookup/suppl/doi:10.1073/pnas.1600311113/-/DCSupplemental.

www.pnas.org/cgi/doi/10.1073/pnas.1600311113

Table 1. Echocardiographic features of SCA mice

Measurement (unit)	WT	Berk-SS	*P* value
$IVSD_d$ (mm)	1.04 ± 0.03	1.13 ± 0.05	0.04
$LVPW_d$ (mm)	0.96 ± 0.03	1.15 ± 0.05	0.005
LVM (mg)	112 ± 6	201 ± 12	<0.0001
$LVID_d$ (mm)	3.67 ± 0.16	4.72 ± 0.11	<0.0001
LVSF (%, vol/vol)	36 ± 3	35 ± 2	0.38

Berk-SS SCA mice (n = 16; 7–8 mo) compared with age- and gender-matched WT controls (n = 14). Data presented as mean ± SEM. Mann–Whitney U test. $IVSD_d$, end-diastolic interventricular septum thickness; $LVPW_d$, end-diastolic LV posterior wall thickness; LVSF, left ventricular shortening fraction.

(42, 43). Furthermore, the combination of modestly increased PAP and diastolic dysfunction confers an increased probability of death in SCA (37, 44) and suggests a hitherto unrecognized unifying etiology.

A comprehensive understanding of SCA-associated cardiovascular pathologies has been hampered partly because the data are inferred from cross-sectional analysis and partly because of limited right heart catheterization studies, given the morbidity associated with invasive tests in SCA. Right heart catheterization studies have been largely restricted to patients with echocardiographically estimated elevation of PAP or those with clinical signs of PH (45, 46). Few studies have been performed with cardiac MRI (CMR) (42, 47, 48), although this noninvasive imaging modality does offer unique advantages. Therefore, the bulk of the cardiac data reported in SCA is based on cross-sectional cardiac imaging using echocardiography. We performed a longitudinal comprehensive cardiac analysis on the Berkeley SCA mouse model (hereafter referred to as Berk-SS) (49), combining state-of-the-art cardiac imaging, electrocardiogram (ECG), cardiac histopathology, and molecular analysis to determine the basis of cardiac dysfunction in Berk-SS mice. Our study demonstrates a distinct restrictive cardiomyopathy superimposed on high-output physiology that results from ischemic cardiomyocyte (CM) loss with secondary microscopic fibrosis and remodeling, predisposing to electrophysiological abnormalities and sudden death.

Results

Berk-SS Mouse Cardiac Features Are Similar to Human SCA. We first wanted to determine if the Berk-SS mouse model mimics the human SCA-related cardiac phenotype. At 7–8 mo of age, echocardiography of Berk-SS and control mice (Table 1) shows Berk-SS mice to have significantly hypertrophied and enlarged LVs, with increased end-diastolic interventricular septal thickness (IVS_d), end-diastolic left ventricular posterior wall thickness, LV mass (LVM), and end-diastolic LV internal dimension ($LVID_d$). LV systolic function as assessed by LV shortening fraction was not different between the two groups, and was thus preserved in the Berk-SS mice, as is the case in human SCA.

Diastolic dysfunction has been reported in adults with SCA (24, 37, 50, 51) and hence was assessed in similarly aged Berk-SS mice using pulsed-wave and tissue Doppler imaging (Fig. 1 and *SI Appendix*, Fig. S1). Pulsed-wave Doppler of mitral valve (MV) flow velocities were consistent with the phenomenon of pseudonormalization seen in early human diastolic dysfunction, and there was a trend toward prolonged isovolumic relaxation time as well. Importantly, the MV IVS E/e′ ratio was significantly higher in Berk-SS mice compared with controls, analogous to humans with diastolic dysfunction and elevated LV end-diastolic pressure. Five aged Berk-SS mice (ages 34–43 wk) and six age- and gender-matched WT mice underwent invasive hemodynamic assessment. Two of the five Berk-SS mice died upon induction of anesthesia but all WT control animals survived to the end of the experimental protocol. Compared with WT, the Berk-SS mice had normal contractility (i.e., dP/dt max) at baseline and at lower levels of β-adrenergic stimulation, consistent with normal systolic function noted by echocardiography in younger Berk-SS mice. However, significantly compromised contractility was evident at higher dobutamine doses. Importantly, we found a trend toward reduced relaxation (τ) (*SI Appendix*, Fig. S2), consistent with the noninvasive data obtained from echocardiography.

Longitudinal Cardiac Imaging Reveals Progressive Left Atrial Enlargement in Berk-SS Mice. To investigate the temporal development of the cardiac phenotype in Berk-SS mice, we performed serial echocardiograms through 8 mo of age. Compared with their age- and gender-matched controls (all mice used in these experiments were males), young Berk-SS mice trended to smaller left atrial dimensions (LAD) initially, likely because Berk-SS mice are relatively "runted" as a consequence of anemia, and weigh ∼1–2 g less than their age- and gender-matched counterparts at all these time points. We observed a progressive increase in the LAD, becoming apparent in the Berk-SS mice at 5 mo of age (2.3 ± 0.1 mm vs. 1.9 ± 0.0 mm, SCA vs. WT, respectively, P = 0.008) and persisting at 8 mo of age (2.6 ± 0.1 mm vs. 2.0 ± 0.2 mm, SCA vs. WT, respectively, P = 0.03) (Fig. 2*B*). Importantly, the LAD did not increase with age in controls and there was no detectable mitral regurgitation in any animal. Furthermore, 8-mo-old SCA mice weighed significantly less (28.5 ± 0.8 g) than their WT counterparts (30.4 ± 0.5 g). The survival curves of all SCA and iron deficiency anemia (IDA) animals used in the experiment are shown in *SI Appendix*, Fig. S3. Representative still images of parasternal long axis M-mode imaging demonstrating left atrial (LA) dimension are shown in Fig. 2*A*.

Progressive LA Enlargement Is Not from Anemia. Chamber dilation can occur from an anemia-related high-output state. To determine if the progressive LA enlargement (LAE) in Berk-SS mice was merely a function of chronic anemia, serial echocardiograms were done on mice with experimentally induced IDA. The hemoglobin of the IDA group of mice was maintained at 7.5 ± 0.1 g/dL (range 5–9 g/dL) from 5 to 8 mo of age. We compared the LAD of 5-mo-old Berk-SS mice to that of 8-mo-old IDA mice to account for the fact that Berk-SS mice become profoundly anemic (average hemoglobin 7.5 g/dL) at ∼2 mo of age, whereas IDA mice did not become anemic until ∼5 mo of age. Thus, both groups were anemic for ∼3 mo at the time of echocardiography. IDA mice developed features of a high-output state (Table 2). Interestingly, the LAD of 5-mo-old Berk-SS mice was still significantly higher than that of the 8-mo-old IDA mice after an equal duration of the anemia (Fig. 2*C*). We also examined the change in LAD (ΔLAD) in the Berk-SS and IDA mice before and after 3 mo of anemia and found that the ΔLAD in 3 mo was also significantly higher in the Berk-SS group compared with the IDA group of animals (P < 0.001) (*SI Appendix*, Fig. S4).

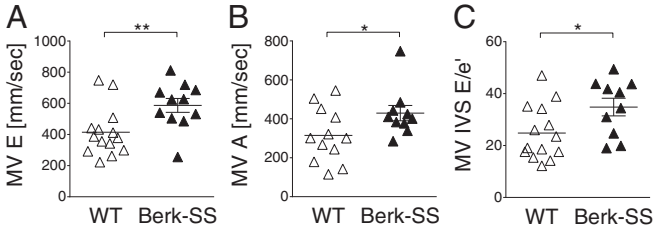

Fig. 1. Sickle mice exhibit evidence of diastolic dysfunction by tissue Doppler imaging (TDI). Six- to 9-mo-old age- and gender-matched sickle (Berk-SS) and WT mice underwent cardiac echocardiography with TDI. Select panels are shown that depict (*A*) mitral valve early filling (MV E), (*B*) mitral valve late filling (MV A), and (*C*) ratio of transmitral E and e′ (MV IVS E/e′). Data shown as mean ± SEM, n = 8–14 mice in WT and 5–10 mice in Berk-SS; Mann–Whitney U test; *$P \leq 0.05$; **$P \leq 0.01$.

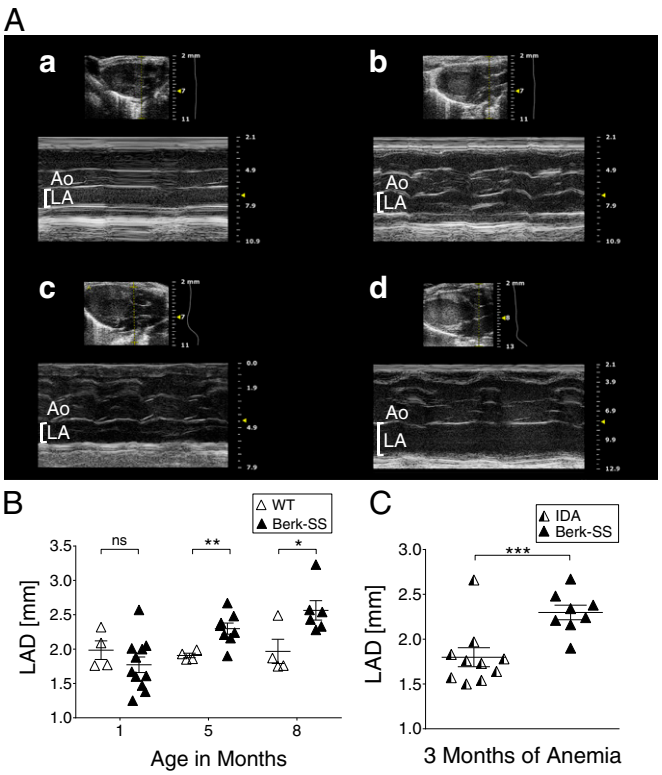

Fig. 2. Sickle mice exhibit progressive LAE compared with their age- and gender-matched WT controls, which is unique to SCA and does not develop in the IDA mice. (*A*) Representative images of parasternal long-axis M-mode imaging through the aortic root and LA demonstrating cross-sectional atrial dilation in a 1- and 8-mo-old sickle cell and WT mouse. The smaller upper image in each set shows the 2D picture of this region of the heart in the parasternal long axis, and the lower image records the movement of each pixel during the cardiac cycle, allowing quantification of structure sizes. Under normal conditions, the LA and aortic root are of approximately equal size. The subpanels are: (*a*) 1-mo-old WT control mouse; (*b*) 8-mo-old WT control mouse; (*c*) 1-mo-old sickle cell mouse (Berk-SS); (*d*) 8-mo-old Berk-SS. Ao, aortic root; LA, left atrium. (*B*) A temporal analysis of LAD by M-mode imaging of WT and Berk-SS mice starting soon after weaning to 8 mo of age. (*C*) Assessment of LAD by transthoracic echocardiography in experimentally induced IDA to achieve hemoglobin levels similar to sickle mice for 3 mo compared with LAD in sickle mice with a similar 3-mo duration of anemia. Data shown as mean ± SEM, $n = 4$ mice in WT, 6–11 mice in Berk-SS, and 10 mice in IDA; Mann–Whitney *U* test; ns, $P > 0.05$; *$P \leq 0.05$; **$P \leq 0.01$; ***$P \leq 0.001$.

In another group of mice, IDA was induced for 6 mo and normal control mice of the same age were followed concurrently. IDA mice had the expected features of a high-output state, specifically a significantly higher $LVID_d$ with preservation of the systolic function, but did not develop LAE compared with normal controls (*SI Appendix*, Table S1). Taken together, we observed significant LAE in Berk-SS mice that was distinct from the ventricular dilation associated with chronic IDA.

Berk-SS Mice Exhibit Evidence of Diffuse Myocardial Fibrosis by CMR. The Berk-SS cardiac phenotype of preserved systolic function with LAE and diastolic dysfunction was quite striking. Because restrictive LV filling can be secondary to myocardial fibrosis, we performed CMR with gadolinium contrast on 6- to 9-mo-old male Berk-SS mice and age- and gender-matched controls. Consistent with the echocardiography data, CMR also showed biventricular dilation and LVH with preserved systolic function in Berk-SS animals (Fig. 3 *A*–*C*). Late gadolinium enhancement (evidence of gross myocardial scarring) was absent. We used contrast-enhanced T1 mapping to measure the proportion of myocardial extracellular volume (ECV), which increases in proportion to the connective tissue fraction and can be regarded as a continuous measurement of the degree of diffuse myocardial fibrosis (52, 53). Interestingly, the percentage myocardial ECV was significantly higher in the Berk-SS mice compared with normal age-matched controls [40.7 ± 2.9% (vol/vol) vs. 29.0 ± 2.8% (vol/vol), $P = 0.006$] (Fig. 3*D*), demonstrating that Berk-SS mice do indeed have evidence of diffuse myocardial fibrosis, which likely results in impaired relaxation, restrictive ventricular filling, and LAE. Our ECV values for normal mice (25 ± 7%) are within the range of published ECV values for mice [22% for juvenile mice and 32% for aged mice (54)]. However, it should be noted that because of various forms of errors in T1 measurement at high field strengths (55), MRI-derived ECV measurements at 7T are best at depicting relative measures of fibrosis between groups rather than absolute values.

Diffuse Myocardial Fibrosis Is Secondary to Sickle Hematopoiesis. To separate potential genetic background influences in the Berk-SS mice from the effects of SCA, we transplanted sickle bone marrow (BM) into lethally irradiated WT mice. To account for potential confounding effects of radiation, mice fully chimeric for sickle hematopoiesis (i.e., exclusively expressing HbS on WT background, designated HbS/WT) were compared with congenic control mice transplanted with WT BM (*SI Appendix*, Table S2). Both groups of mice were followed for 8–9 mo and evaluated using CMR and echocardiography. Hearts that were normal anatomically and functionally before HbS transplant developed findings that mirrored the features of the nontransplanted Berk-SS mice (*SI Appendix*, Tables S3 and S4), specifically ventricular dilation, LVH, and preserved systolic function. Increased proportion of myocardial ECV was seen in the HbS/WT chimeras, demonstrating that diffuse cardiac fibrosis is a unique feature that develops in SCA and is secondary to sickle hematopoiesis (*SI Appendix*, Fig. S5).

Berk-SS Mice Show Evidence of Microscopic Multifocal Ischemic Changes and Fibrosis. Histopathologic evaluation was performed to dissect the mechanisms underlying Berk-SS restrictive physiology. H&E-stained sections of Berk-SS mouse hearts showed LAE as early as 3 mo of age. After a similar duration of anemia, the IDA mouse hearts exhibited ventricular dilation but not LVH (Fig. 4*A*), consistent with the echocardiography data. Although no gross infarction was evident in the ventricles of Berk-SS mice, myocardial tissue exhibited multifocal areas of ischemic changes of varying stages microscopically (Fig. 4*B*). Early ischemic changes were characterized by loss of cardiac cross striations and decreased CM cytoplasmic eosinophilia (Fig. 4 *B*, *b*). Late and more severe ischemic changes included myocytolysis and occasional vacuolar degeneration (Fig. 4 *B*, *d* and *e*). In a few cases, microvessels occluded/congested with sickled RBCs were found adjacent to these microscopic ischemic lesions (Fig. 4 *B*, *f*). No ischemic changes or microvascular occlusions were present in the WT controls (Fig. 4 *B*, *a* and *c*). CM loss was multifocal and distributed randomly, being replaced by areas of fibrosis, seen as patches of Sirius red and Masson's Trichrome

Table 2. Echocardiographic features of IDA mice

Measurement (unit)	WT	IDA	*P* value
$IVSD_d$ (mm)	0.98 ± 0.03	1.02 ± 0.07	0.34
$LVPW_d$ (mm)	0.92 ± 0.05	0.86 ± 0.05	0.23
LVM (mg)	102 ± 5	128 ± 13	0.09
$LVID_d$ (mm)	3.65 ± 0.20	4.20 ± 0.11	0.03
LVSF (%, vol/vol)	33 ± 3	29 ± 3	0.14

IDA mice ($n = 10$; 8-mo-old, 3 mo of IDA) compared with age- and gender-matched WT controls ($n = 7$). Data presented as mean ± SEM. Mann-Whitney *U* test.

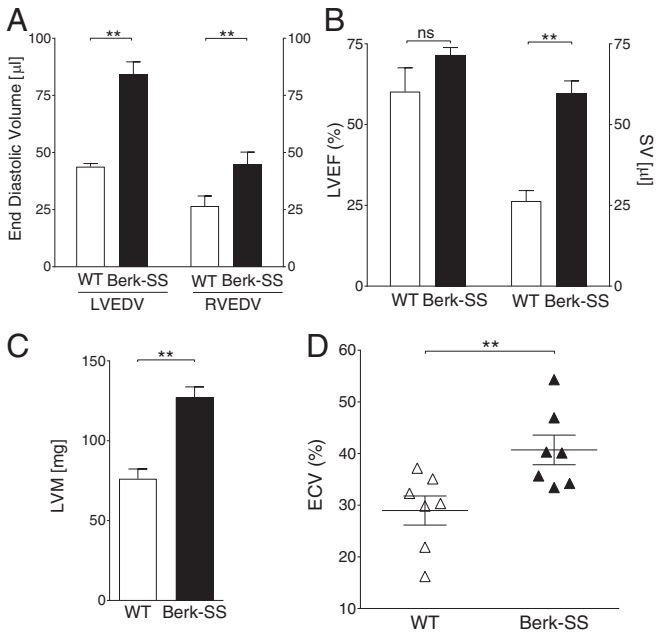

Fig. 3. Sickle mice exhibit LV hypertrophy and dilation with preserved systolic function but increased myocardial fibrosis by CMR. Six- to 9-mo-old age- and gender-matched sickle (Berk-SS) and WT mice underwent CMR. Panels depict (*A*) left and right end-diastolic volumes (LVEDV and RVEDV, respectively); (*B*) LV ejection fraction (LVEF) and stroke volume (SV); (*C*) LVM; and (*D*) myocardial extracellular volume (ECV%) measured by contrast-enhanced T1 mapping. Data shown as mean ± SEM n= 3–7 mice in WT and 7–9 mice in Berk-SS; Mann–Whitney *U* test; ns, $P > 0.05$; $^{**}P \leq 0.01$; $^{***}P \leq 0.001$.

staining (Fig. 5). These microscopic fibrotic foci in the myocardium were absent in WT mice, and were found to be scattered across multiple sections of the myocardium with intervening normal hypertrophied myocardial tissue, complicating quantification. The total hydroxyproline content of the atria and the ventricles-interventricular septum of age- and gender-matched SCA mouse hearts was significantly higher in the SCA mice than WT controls (*SI Appendix*, Fig. S6), although the hydroxyproline concentration was not (and indeed lower), likely because of the pronounced intervening cardiomyocyte hypertrophy seen in SCA hearts compared with controls. Furthermore, Prussian blue and Congo red stains did not show evidence of iron overload or amyloid deposition in the sickle myocardium, respectively (*SI Appendix*, Fig. S7). Collectively, Berk-SS hearts were characterized by both myocardial LVH and extracellular matrix expansion from fibrotic foci, likely a sequelae of microvascular ischemic events and consistent with the increased ECV seen on CMR.

Berk-SS Mouse CMs Exhibit Hypoxia/Ischemia-Related Mitochondrial Ultrastructural Changes and Contracted Sarcomeres with Significant Remodeling. EM showed enlargement of Berk-SS mitochondria with variation in size, shape, and distribution compared with the regularly distributed and mostly elongated mitochondria of WT controls (Fig. 6 *A*–*D*). Some Berk-SS mitochondria appeared swollen, with fewer and less-compacted cristae, and there were areas of matrix lysis and elongated cristae, findings associated with prolonged ischemia. Other observations distinct to the Berk-SS mice included unevenly widened myofibrils with large spaces between membranes of the sarcoplasmic reticulum (SR) and sarcomeres around the mitochondria. Sarcomeres of Berk-SS CMs often had indistinguishable/invisible I bands with a significantly shorter mean sarcomere length in Berk-SS mice compared with controls (1.76 ± 0.03 μm vs. 2.01 ± 0.01 μm, respectively, $P < 0.0001$) (Fig. 6 *D*–*F* and *SI Appendix*, Fig. S8), suggesting alterations in cross-bridge cycling, particularly during relaxation.

The Myocardial Transcriptome Shows an Increased Hypoxic, Oxidative, Profibrotic Signature with Down-regulation of Genes Associated with Electrophysiological Function. To evaluate the cardiac stress state and adaptations to the effects of SCA, we evaluated gene-expression patterns in normal and Berk-SS mice. Berk-SS mice exhibited a very distinct signature compared with normal animals (*SI Appendix*, Fig. S9*A*), with 334 genes being up-regulated and 147 down-regulated (using 1.5-fold and <0.05 false-discovery rate cut-offs). Functional enrichment analysis showed particularly strong enrichment of genes involving angiogenesis, extracellular matrix, and circadian rhythm, as well as responses associated with oxidative stress, hypoxia, and TGF-β signaling (Fig. 7*A*) that are congruent

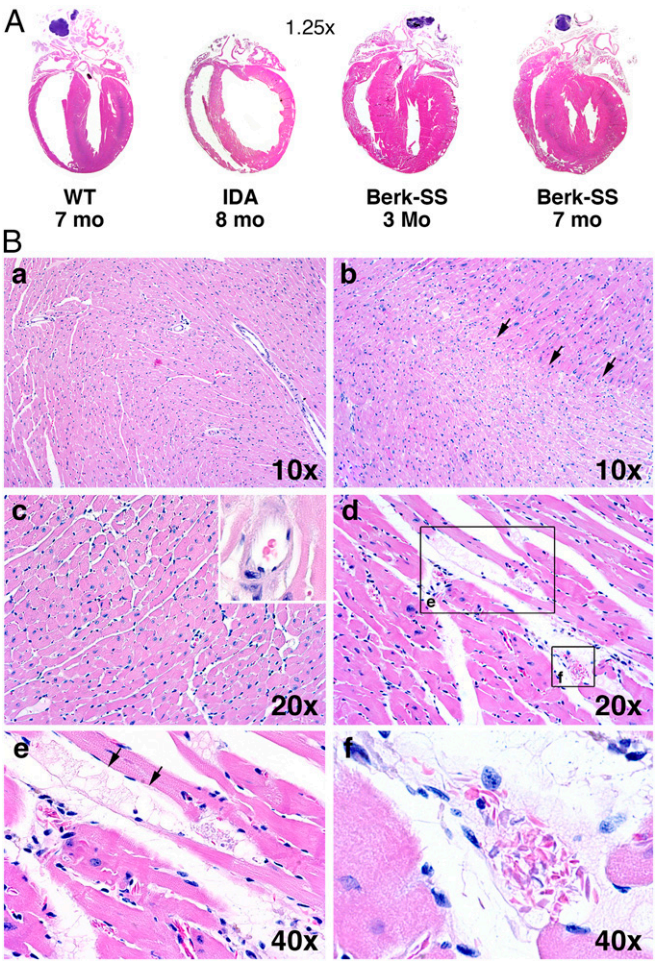

Fig. 4. Sickle mice exhibit biventricular hypertrophy and microscopic multifocal ischemic changes and fibrosis. (*A*) Representative H&E-stained four-chamber views of WT, IDA, and sickle (Berk-SS) mouse hearts. Compared with an age- and gender-matched WT control, the 8-mo-old IDA mouse heart exhibits ventricular dilation but not hypertrophy after 3 mo of anemia. Biventricular hypertrophy and LA dilation are noted as early as 3 mo of age in the Berk-SS mouse. These findings worsen with age as evident in the 7-mo-old Berk-SS mouse. (*B*) H&E-stained mouse myocardium. Compared with an age- and gender-matched WT control (*a*), an 8-mo-old male Berk-SS mouse shows early ischemic changes characterized by loss of cross striations and decreased cardiomyocyte cytoplasmic eosinophilia (black arrows) (*b*). Late and more-severe ischemic changes, such as vanishing dead cardiomyocytes, are also noted in the Berk-SS mouse (*d* and *e*), and an occluded/congested microvessel with sickled RBC is noted adjacent to these ischemic changes (*f*, *Inset*). Microvessels are patent in the WT mouse (*c*, *Inset*).

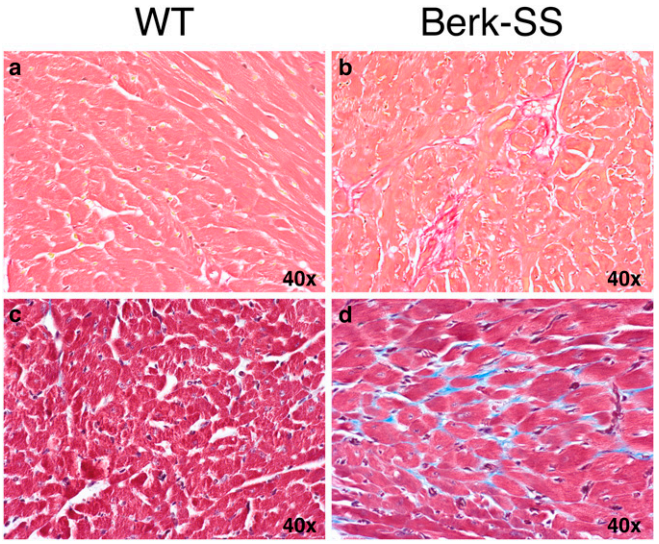

Fig. 5. Patchy microscopic fibrosis is seen in sickle mice hearts. Sirius red (*A* and *B*) and Masson's trichrome (*C* and *D*) staining of the myocardium of 8-mo-old sickle (Berk-SS) and WT mice. Patchy microscopic fibrosis can be seen in the Berk-SS mouse (*B* and *D*) but not the age- and gender-matched WT control mice (*A* and *C*).

with the imaging and histopathology data. Down-regulated genes were particularly enriched for ion channel transport and fatty acid-associated metabolism. The detailed Gene Ontology listing with the individual gene hits is available in *SI Appendix*, Table S5. Connective-tissue growth factor (CTGF), a fibrotic factor known to trigger synthesis of extracellular matrix in the myocardium in response to TGF-β, was found to be up-regulated by 3.5-fold by RNA-seq. Increased CTGF protein was confirmed by immunohistochemistry with interspersed areas of pronounced focal CTGF staining in regions of CM loss (Fig. 7*B*). We also noted a 15-fold up-regulation of δ-aminolevulinic acid synthase (*ALAS2*), a key enzyme involved in heme synthesis. It is noteworthy that of the down-regulated genes, at least 31 are involved in ion and voltage transport and regulation, all of which are critical for cardiac function and conduction (heat map shown in *SI Appendix*, Fig. S9*B*). Gene network analysis (Fig. 8) showed dramatic loss of expression of an extensive set of genes associated with maintenance of electrophysiological and structural integrity of the heart. Seven key down-regulated genes [carnitine palmitoyltransferase (*CPT*)*1A*, *CPT2*, sodium voltage-gated channel beta subunit 4 (*SCN4B*), A-kinase anchoring protein 9 (*AKAP9*), sodium voltage-gated channel alpha subunit 4 (*SCN4A*), potassium voltage-gated channel subfamily J member 2 (*KCNJ2*), calcium voltage-gated channel subunit alpha1 S (*CACNA1S*)] whose dysfunction is associated with prolonged QT interval, arrhythmias, and sudden cardiac death are highlighted.

Berk-SS Mice Develop Corrected QT Prolongation and Widening of QRS Associated with Cardiac Ischemic Events and Fatal Arrhythmias with Sudden Death. ECGs were obtained weekly from 5 to 8 wk of age. Like humans with SCA, Berk-SS mice also experience sudden death, with increased mortality in the first 3–4 mo after weaning that occurs without forewarning signs of distress. Survival curves for our WT and Berk-SS mice are shown in *SI Appendix*, Fig. S3, confirming the high mortality in SCA mice and none in the WT mice during the window where ECG experiments were performed. Corrected QT (QTc) and QRS interval prolongations were noted as early as 5 wk of age compared with age- and gender-matched WT controls (*SI Appendix*, Table S6). QTc prolongation persisted to 8 wk of age in the surviving mice (99 ± 3 ms vs. 81 ± 3 ms in Berk-SS vs. WT controls, respectively; $P = 0.0003$) (Table 3). Over the ECG surveillance month, the mortality rate among the sickle mice was about 40%, consistent with the overall mortality in our Berk-SS mouse colony (56). All WT mice survived through adulthood. Antemortem telemetry was serendipitously obtained for two 2-mo-old Berk-SS mice that were found to be sluggish during daily mouse assessment, despite being active and well-appearing the day prior, and who died while on the ECG platform. Compared with a normal WT control (Fig. 9, panel 1), the telemetry of the first mouse was significant for ST depression, suggestive of an ischemic insult before death (Fig. 9, panel 2). In the second mouse (Fig. 9, panels 3–5), initial recordings showed that the mouse had a slower heart rate and P-wave irregularity (Fig. 9, panel 3), which then progressed to heart block with atrial flutter with 4–5:1 AV conduction (Fig. 9, panel 4), and eventual ventricular fibrillation (Fig. 9, panel 5). This mouse had a very prolonged QTc on the day of his death at 119 ms, nearly 1.5-times that of age- and gender-matched WT controls. Interestingly, three other 6-wk-old

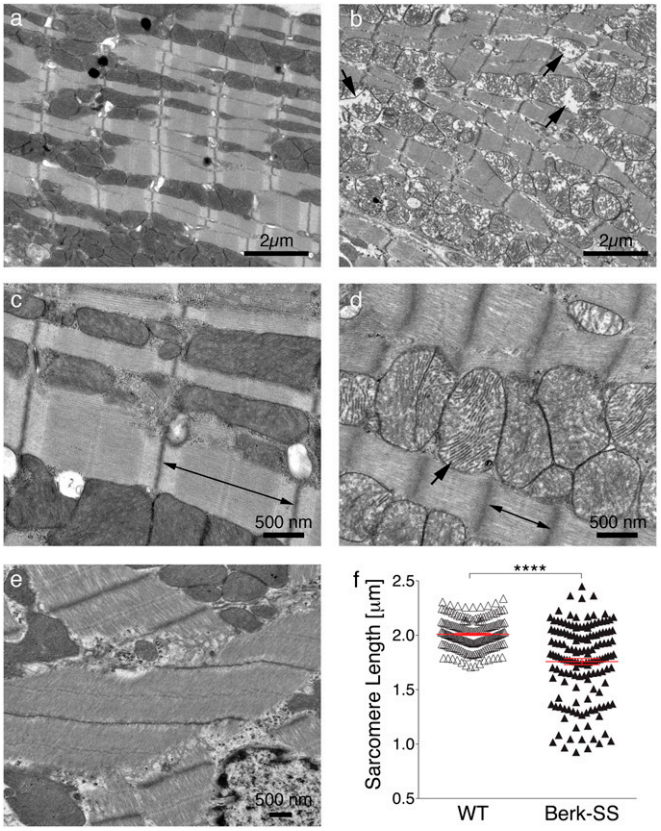

Fig. 6. Sickle cardiomyocytes exhibit hypoxia/ischemia-related mitochondrial ultrastructural changes, contracted sarcomeres, and chaotic remodeling. Representative EM images of WT and sickle mouse LV posterior wall myocardium. Compared with WT control (*A* and *C*), a subset of cardiomyocytes in an 8-mo-old sickle mouse show ultrastructural abnormalities (*B*, *D*, and *E*). Electron lucent areas between mitochondria and sarcomeres, and membranes of the SR and sarcomeres are noted (*B*, arrows). Mitochondria are hypertrophied, more abundant, more rounded, with less densely packed and often disrupted cristae (*D*, arrow). Sarcomeres in some of the sickle cells were contracted and hence shorter in diastole (*D*, double-headed arrow) compared with WT (*C*, double-headed arrow). Chaotic cardiomyocyte remodeling is noted in a 2-mo-old Berk-SS mouse (*E*). Sarcomere lengths of two, 8-mo-old sickle (Berk-SS) and age- and gender-matched WT controls are shown in *F*. Data shown as mean ± SEM, $n = 187$ sarcomere in WT and 150 sarcomere in Berk-SS, two mice per group, Mann–Whitney *U* test, $^{****}P \leq 0.0001$.

A

Extracellular Matrix	P value
Extracellular matrix organization ↑	1.65E-05
Cell-matrix adhesion ↑	3.40E-02
Extracellular matrix binding ↑	2.53E-05
Cellular response to transforming growth factor beta stimulus ↑	2.22E-03
Angiogenesis	
Vasculature development ↑	2.44E-11
Angiogenesis ↑	2.16E-10
Lipid Metabolism	
Response to lipid ↑	4.80E-07
Abnormal circulating free fatty acid levels ↓	9.18E-06
Glycerolipid metabolic ↓	1.62E-03
Neurotransmission	
Abnormal circadian period ↑	8.55E-04
Ion channel activity ↓	6.70E-05
Serotonergic synapse ↓	1.97E-03

B

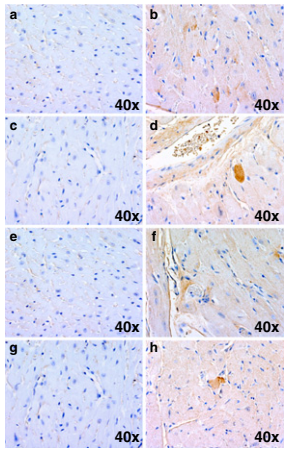

Fig. 7. (*A*) Gene Ontology pathways that are differentially regulated between WT and Berk-SS mouse myocardium (n = 3 WT and 3 in Berk-SS), following a sickle myocardial transcriptome (with associated P values) compared with WT myocardial transcriptome; arrows indicate up- or down-regulated pathways in the sickle myocardium. (*B*) Immunohistochemistry staining of CTGF in mouse myocardium. Compared with age- and gender-matched WT myocardium (*a*, *c*, *e*, *g*), an 8-mo-old Berk-SS mouse shows increased overall background expression (*b*, *d*, *f*, *h*) with several areas of pronounced focal staining (perivascular regions and areas of myocyte loss).

Berk-SS mice that died suddenly (where ECGs were not recorded in the immediate antemortem period) were noted to have significant prolongation in their QTc on the ECG obtained 1–3 d before their death (Fig. 9, panel 6). These data suggest that ischemia, with evidence present on myocardial histology, and arrhythmias secondary to asymptomatic QTc prolongations, may precede sudden death, although the ECG changes noted in the mice dying during monitoring could be a nonspecific finding of impending death. Interestingly, the electrical anomalies in the Berk-SS mice precede the functional changes first manifested as LA dilation at 5 mo of age, suggesting that the ECG changes are not merely a consequence of established cardiomyopathy.

Discussion

Herein, we show the development of a distinct SCA cardiomyopathy superimposed on changes associated with chronic anemia and characterized by diffuse myocardial fibrosis and restrictive physiology. Consistent with human data, SCA mouse echocardiographic and CMR data show dilated and hypertrophied ventricles with preserved systolic function, findings attributable to the chronic anemia-associated high-output state (31–35). Using a chronic IDA model with the same duration and degree of anemia, we show that the SCA cardiac phenotype is not caused primarily by chronic anemia; rather, sickle hematopoiesis-associated focal microvascular occlusions, ischemia, and oxidative stress compound the effect of chronic anemia. Scattered microscopic CM loss, myocardial fibrosis, and significant CM remodeling likely contribute to this distinct cardiomyopathy and predispose to electrophysiological abnormalities, leading to arrhythmias and sudden death. Although some ultrastructural changes seen in the SCA myocardium are reminiscent of those previously reported in chronic anemia-associated myocardial hypoxia (i.e., enlarged mitochondria with variation in size, shape, and distribution and unevenly thickened myofibrils) (57–60), EM demonstrated features distinct to SCA, including mitochondria with fewer and less-compacted cristae, abnormalities of the SR, and contracted sarcomeres, features that may contribute to diastolic dysfunction and an arrhythmogenic milieu.

LAE was quite prominent in mice with SCA. LAE is clinically significant because it has been shown to predict and foreshadow adverse clinical cardiovascular outcomes in other conditions where

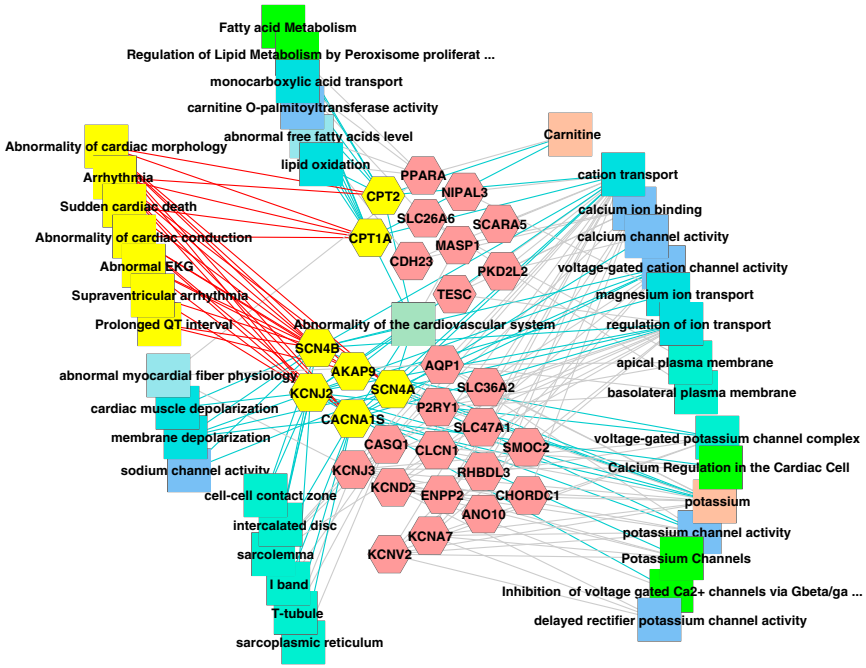

Fig. 8. Biological network analysis of the SS down-regulated genes in the heart showed dramatic loss of expression of an extensive set of genes associated with maintenance of the electrophysiological and structural integrity of the heart. RNAseq showed that 31 ion channel genes and genes associated with electrophysiologic function were down-regulated in Berk-SS mouse myocardium compared with WT (n = 3 WT and 3 in Berk-SS). The seven key down-regulated genes (yellow: *CPT1A*, *CPT2*, *SCN4B*, *AKAP9*, *SCN4A*, *KCNJ2*, *CACNA1S*) are associated with arrhythmias and sudden cardiac death. The cardiac networks they affect and how they interact with the rest of the down-regulated genes associated with rhythm dysfunction, including prolonged QTc, are shown.

Table 3. ECG parameters of SCA mice

Measurement (unit)	WT	Berk-SS	*P* value
P duration (ms)	14.7 ± 0.5	15.3 ± 0.8	0.6
PR interval (ms)	33.2 ± 0.6	32.8 ± 0.8	0.71
RR interval (ms)	79 ± 2	83 ± 5	0.05
Heart rate (bpm)	763 ± 7	730 ± 12	0.05
QRS duration (ms)	12.2 ± 0.5	14.6 ± 0.6	0.01
QTc (ms)	81 ± 3	99 ± 3	0.0003

Berk-SS SCA mice ($n = 10$; 2 mo) compared with age- and gender-matched WT controls ($n = 8$). Data presented as mean ± SEM. Multiple *t* tests, Holm–Sidak correction. bpm, beats per minute.

diastolic dysfunction is a predominant mechanism (61–64). The LAE in our SCA mice was not associated with mitral regurgitation and was both early and exaggerated. Importantly, LAE was significantly greater in SCA than IDA mice, indicating that the phenotype is more complex than hyperdynamic physiology because of anemia. We propose that in our SCA mice, LAE is a downstream consequence of microscopic myocardial fibrosis, leading to ventricular diastolic dysfunction and in turn, impaired LA emptying and LA hypertension. Restrictive LV filling and LA hypertension may lead to elevated pulmonary venous pressure, a feature associated with increased TRV in patients with SCA (18, 65, 66).

In addition to LAE, another significant finding in our SCA model is LV diastolic dysfunction with preserved systolic performance. Importantly, this phenotype is reproduced in normal mice transplanted with sickle bone marrow. This SCA cardiomyopathy is not a "classic" restrictive cardiomyopathy, the latter characterized by diastolic dysfunction and atrial dilation in the presence of normal atrioventricular valve anatomy, ventricular wall thickness, and systolic function. Restrictive cardiomyopathy diagnostic criteria typically exclude ventricular dilation and hypertrophy, both features of our model (67–69). Interestingly, diastolic dysfunction is also prevalent in human SCA and has been considered to be an independent risk factor for early mortality (37). The exact cause of diastolic dysfunction in SCA is not well understood, but we show that it cannot be significantly attributed to chronic anemia. Most reports of diastolic dysfunction in humans with chronic anemia are in the setting of comorbidities, such as chronic kidney disease (70, 71), diabetes mellitus (72), and coronary artery disease (73), whereas reports of diastolic dysfunction developing in otherwise healthy adults who are chronically anemic are inconsistent (74).

Of the childhood cardiomyopathies, restrictive cardiomyopathy has the highest rate of sudden cardiac death, with survivors demonstrating findings of pulmonary hypertension as a result of LA hypertension. The severity of the compounded effects of anemia and restrictive physiology in SCA patients is thus of significant concern and warrants careful study. Anemia-related LVH is seen in SCA and it is conceivable that the chronic anemia-associated LVH progressively increases myocardial oxygen demand and oxygen extraction, which subsequently results in microvascular sickling and microvasculature-related ischemic events, characterized at the microscopic level by CM loss and myocardial fibrosis. Increased oxidative stress likely further compounds this effect. Similar, albeit milder changes, have been described in IDA animal models (59, 60, 75, 76). It may be that these changes are more severe in SCA because of the added disadvantage of sickling in the microvasculature and increased oxidative stress, both evident in our transcriptome analyses. Also evident is a down-regulation of circadian rhythm genes. Experimentally induced deficiency of circadian rhythm genes in mice (*SCN*, *CK1ε*, *Per2*, and *CLOCK*) have been shown to alter cytokine and immune responses, shorten lifespan, increase fibrosis, tumor progression, and result in cardiac disturbances, including myocardial infarction and altered cardiac hypertrophic pathways. Hence, future studies are warranted to determine the role of down-regulated circadian rhythm genes in modulating clinical phenotype in SCA.

Repeated sickling-related microvascular ischemic events, increased oxidative stress and microscopic focal fibrosis, can result in significant remodeling and a stiff LV with diastolic dysfunction. It has been recently reported that some degree of focal LV fibrosis measured using late gadolinium enhancement can be seen in young adults with SCA by CMR (42, 48), and LV fibrosis was also reported in autopsies of young adults with SCA who died suddenly (77). Moreover, recent reports suggest dysregulated profibrotic pathways are up-regulated in SCA in general, as polymorphisms in TGF-β signaling pathway genes have been found in this patient population (78). We have recently reported hyperangiotensinemia in mice and humans with SCA (79). It would be worth exploring whether angiotensin signaling, which is known to up-regulate TGF-β1 signaling, may also contribute to the cardiac hypertrophy and remodeling seen in SCA mice, in contrast with the IDA mice. Our SCA mouse myocardium gene-expression profile is consistent with this concept, showing strong enrichment of genes involving angiogenesis and extracellular matrix, including CTGF, a fibrotic factor known to trigger synthesis of extracellular matrix in the myocardium in response to TGF-β1. One notable finding was remarkably increased expression of a heme synthetic

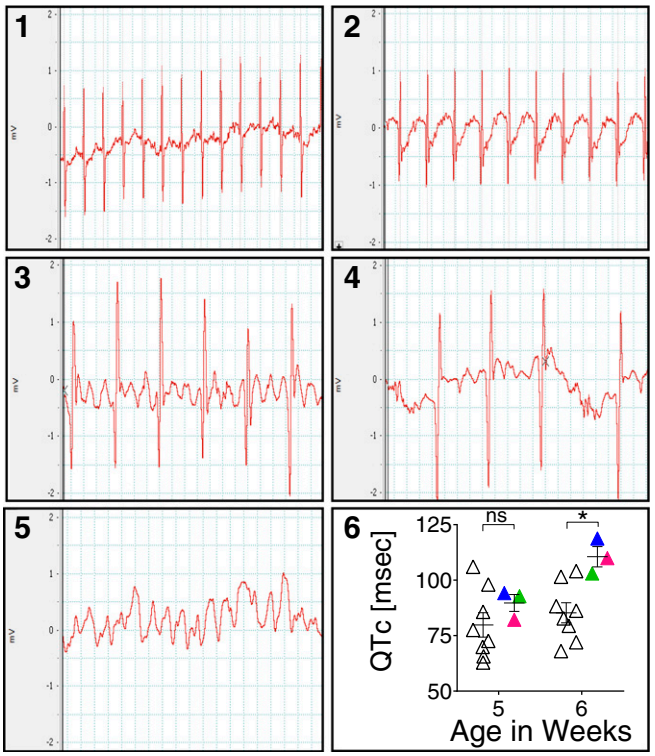

Fig. 9. QTc prolongation, cardiac ischemic events, and fatal arrhythmias are evident in antemortem EKG tracings of sickle mice. Compared with the normal sinus rhythm in a 2-mo-old WT control (*1*), antemortem EKG tracings of an age-matched Berk-SS mouse shows ST depression (*2*). Another 2-mo-old Berk-SS mouse's antemortem EKG tracings show slower heart rate and P-wave irregularity (*3*), which progressed into outright atrial flutter with 4–5:1 AV conduction (*4*), and eventual ventricular fibrillation (*5*). Sudden and significant QTc prolongation of three 6-wk-old Berk-SS male mice few days before their death (filled triangle) compared with their age- and gender-matched WT (open triangles) controls (*6*). Data shown as mean ± SEM $n = 8$ mice in WT and 3 mice in Berk-SS; Mann-Whitney *U* test; ns, $P > 0.05$; *$P \leq 0.05$.

enzyme ALAS2. Recently, increased myocardial ALAS2 expression has been shown to potentiate ischemic injury and to be associated with heart failure (80, 81). The finding of ALAS2 up-regulation in SCA is consistent with the myocardial ischemia observed on histopathology and EM.

Although we used IDA mice to control for anemia, which do not have the confounding effects of hemolysis, ineffective erythropoiesis, and iron overload, this model does suffer from iron deficiency. It may be worthwhile comparing other chronic anemia models that are not iron deficient, such as thalassemia intermedia mice on a low-iron diet (to prevent iron overload that otherwise develops on an iron-replete diet in thalassemia) in future studies.

In summary, using the SCA mouse model, we demonstrate a distinctive sickle cardiomyopathy where restrictive physiology is superimposed on chronic anemia and predisposes to sudden death. Mechanistically, ischemic-scattered CM loss, myocardial fibrosis, and significant cardiac remodeling appears to underlie this restrictive physiology and abnormal electrophysiology. In addition, our studies show that restrictive physiology can be diagnosed by noninvasive methodology, which is particularly desirable in monitoring patients with SCA. Our genetic studies point to the importance of up-regulated fibrotic pathways and secondary consequences, including dysregulated ion channels. Equipped with this knowledge, the SCA mice are a valuable resource for preclinical study of this phenomenon with the ultimate goal of a better understanding of—and treatment for—the cardiac complications of SCA.

Materials and Methods

Experimental Mice. Berkeley SCA mice [Tg(Hu-miniLCRα1GγA$\gamma\delta\beta^S$) Hba^0//Hba^0 Hbb^0//Hbb^0] (49) are genetic knockouts for mouse β- and α-globin genes that exclusively express human α and β^S (HbS) postnatally. WT control Bl/6 congenic mice were either C57BL/6 (CD45.2+) or Bl/6.BoyJ (CD45.1+). In some experiments, we performed hematopoietic stem cell transplantation of pooled Berk-SS donor BM into WT mice. The Berk-SS mice were derived from five different genetic strains of mice and have been backcrossed to C57BL/6 mice for six generations, and thus can be used as donors for transplant into Bl/6 mice. Briefly, lethally irradiated (1,175 cGy) Bl/6.Boy J (CD45.1) recipient mice were transplanted with either Berk-SS or C57BL/6 (CD45.2) BM in a 1:6–7 donor to recipient ratio. Only mice showing complete donor chimerism [>99.5% donor cells, compared to 0.5% residual host cells] were followed in the experiments. IDA was induced in cohorts of WT (C57BL/6) mice using a low-iron chow (Modified AIN-93M, containing 8 ppm of iron) and paper bedding to maintain hemoglobin levels between 5 and 9 g/dL, which corresponds to the hemoglobin profile of the SCA mice in our colony. A control age-matched cohort was placed on iron-replete chow (39 ppm of iron). Per protocol, weekly complete blood counts were monitored to ensure chronic anemia; if animals in the IDA group had hemoglobin values below 5 g/dL, iron-deficient chow was replaced with regular chow for a week. If animals had hemoglobin levels greater than 9 g/dL in the IDA group, a 250- to 300-μL phlebotomy was performed that week. All animals were maintained in the Cincinnati Children's Research Foundation's vivarium using protocols approved by the Institutional Animal Care and Use Committee.

Hematological Assessment. Whole blood was obtained from animals via phlebotomy from the inferior vena cava into tenth volume 0.1 M sodium citrate. Aliquots of this whole blood were used for complete blood count determinations using a Hemavet 950FS (Drew Scientific) analyzer.

Echocardiography. Two-dimensional and M-mode transthoracic echocardiography was performed as previously described using a Vevo 2100 Micro-Imaging system (VisualSonics) equipped with a 40-MHz high-frequency transducer (82). The imaging platform was warmed to prevent hypothermia and sickling in SCA mice.

Invasive Hemodynamics. Invasive LV pressure measurements were made in inaction/ketamine-anesthetized mice using a high-fidelity pressure catheter (Transonic Scisense) under baseline conditions and in response to graded doses of the β-adrenergic agonist dobutamine.

CMR. CMR was performed in the Cincinnati Children's Imaging Research Core on a 7 Tesla Bruker MR scanner using a custom-made single-turn-solenoid RF coil. Mice were anesthetized with 1.5% (vol/vol) isoflurane. Physiological monitoring, ambient temperature, and cardiac triggering were done using an MR-compatible monitoring and gating system (Model 1025, SA Instruments), and the data were processed using Segment v1.9 (segment.heiberg.se) for volumetric analysis (83), and custom-designed software (MATLAB, 8.3 MathWorks) for diffuse fibrosis. CMR was used to quantify fibrosis, chamber volumes, and systolic function. Chamber volumes were measured using short-axis cine images using a FLASH sequence, which included slice thickness 1.0 mm, matrix size 256 × 256, and in-plane resolution 117 × 117 μm^2, TE/TR 3/10 ms, flip angle 20°, and segments = 1. Approximately 15–20 cine frames were acquired during the cardiac cycle, depending on heart rate, with a temporal resolution of 10 ms. Systolic strain was measured using tagged images acquired in the midventricle using an RF pulse train, as previously described (84). Tag separation was 0.8 mm, field-of-view was 34 × 34 mm^2, and slice thickness was 1 mm, with matrix 256 × 128. Diffuse fibrosis was measured by quantifying myocardial T1 before and after injecting a bolus of gadolinium (0.2 mmol/kg diluted in saline solution in a 1:10 ratio) intraperitoneally. A double-gated, Look-Locker sequence was used. Twenty phase-encoding lines were acquired at 20 different inversion times [TI = multiples of 2 RR (time interval between consecutive R-waves in the ECG) for precontrast T1, TI = multiples of 1 RR for postcontrast T1]. All images were acquired in the short-axis plane at end diastole. Diffuse fibrosis was quantified in terms of T1-dependent ECV of the myocardium (85).

For T1 measurement we used an inversion-recovery T1 (Look-Locker) method as implemented in a previous study (86). The following steps were taken to minimize errors resulting from ECG variations. (*i*) We reduced the total scan time for T1 measurement to less than 15 min (64 k-space lines) by not acquiring multiple scans for signal averaging. Typically, the total drift of the RR during this period was less than 10% (msec/msec) of the initial RR value. The loss in SNR as a result of not signal averaging was compensated by limiting spatial resolution. (*ii*) The experiment was stopped if the RR drift was more than 10% of its initial value. In such cases, readjusting the anesthetic gas volumes enabled steady RR.

Electrocardiography. A noninvasive ECG recording system (ECGenie, Mouse Specifics) was used to acquire ECGs from conscious mice during the daytime, as previously described (87). Because even modest handling of mice may induce alterations in their heart rate (88), each mouse was permitted to acclimate for at least 10 min, and recording commenced when at least three of the mouse's paws were in full contact with the leads.

Histology. Mice were killed, dissected, and their hearts isolated carefully and submerged in cold PBS for 10 s to remove excess blood. The hearts were then perfused with a cardioplegic solution (68 mM NaCl, 50 mM KCl, 11 mM glucose, 12 mM $NaHCO_3$, 30 mM 2,3-butanedione monoxime, 10 mM EGTA, 1 μM nifedipine, and 10 units/mL heparin, pH titrated to 7.4). Thereafter, the hearts were perfused with 15 mL of 10% (vol/vol) formalin, fixed for at least 48 h, embedded in paraffin, and processed for histological analysis. Four- to 6-μm sections of the paraffin-embedded hearts were stained with H&E, Masson's trichrome, Picrosirius red, Prussian blue, and Congo red stains by the Cincinnati Children's Hospital Pathology Core Facility. All staining procedures were performed using the Ventana Symphony staining platform (Ventana Medical Systems). Stained sections were reviewed with a board-certified pathologist who was blinded to the mouse genotype.

Determination of Myocardial Hydroxyproline Content. Myocardial hydroxyproline content was analyzed as previously described (89, 90). Briefly, the atria were separated from the ventricles and intraventricular septum. The ventricles and septum were cut into smaller pieces, which were weighed and hydrolyzed overnight with 6 N hydrochloric acid in an oven at 100 °C. The samples were thereafter desiccated in the oven at 50 °C using a desiccator containing sodium hydroxide pellets. The tissue was kept under vacuum until dry, and thereafter resuspended in 5 mM hydrochloric acid. Aliquots of each hydrolyzed tissue sample were then combined with water, chloramine T solution, hydroxyproline assay buffer, and Ehrlich's reagent. After incubating the samples for 20–25 min at 55 °C, and subsequently cooling them to room temperature, sample absorbance was read at 558 nm. Trans-4-hydroxy-l-proline standard (Sigma; ranging from 0 to 4 μg) was used to generate a standard curve to determine hydroxyproline content. Readings were subsequently normalized to starting tissue weight.

Immunohistochemistry. Paraffin-embedded heart sections (4 μm) were deparaffinized, hydrated, and incubated in 3% (vol/vol) hydrogen peroxide

solution for 10 min and rinsed, then blocked with 10% (vol/vol) normal goat serum + 0.3% Triton X-100 in PBS (hereafter referred to as "block solution") for 1 h at room temperature. Sections were then incubated in CTGF primary antibody (Ab6992, Rabbit polyclonal anti-mouse, 1:600 dilution in block solution) overnight at 4 °C. On the next day after washing, slides were incubated with biotinylated goat anti-rabbit secondary antibody (diluted in 1:200 in block solution) for 1 h at room temperature, followed by incubation in ABC solution for 1 h VECTASTAIN Elite ABC kit (Vector Laboratories). After rinses, sections were stained with DAB (SK-4100, Vector Laboratories) for 5 min, and rinsed in water and counterstained with hematoxylin. Finally, sections were dehydrated, then cleared in xylene and mounted using Histomount. Stained sections were reviewed with a board-certified pathologist who was blinded to the mouse genotype and experimental arm.

Transmission Electron Microscopy and Sarcomere Length Measurement. Hearts of previously anesthetized (isoflurane) mice were perfused through the LV apex and then the right ventricle (RV) with 1% glutaraldehyde/2% (vol/vol) paraformaldehyde in cardioplegic solution (100 mM KCl, 5% dextrose in PBS) followed by 1% glutaraldehyde/2% (vol/vol) paraformaldehyde in 0.1 M cacodylate buffer (pH 7.3), dissected out, and dropped into ice-cold glutaraldehyde/paraformaldehyde/cacodylate solution. Next the LV and RV free walls, septum and apex were separated and, after being divided into 1-mm^3 fragments, and further fixed for 1–4 d at 4 °C, subsequently they were postfixed in 1% osmium tetroxide/cacodylate buffer, dehydrated in acetone series, and embedded in an EMbed812 resin mixture. Ultrathin (70 nm) sections were counterstained with uranium and lead salts and examined using the Hitachi 7600 transmission electron microscope at accelerating voltage of 80 kV. Images were acquired with an AMT digital camera. The sarcomere length (distance between two thick myosin filaments) was measured on sections from each group of young adult or old, WT, or Berkeley sickle mice, for a total of 1,295 sarcomeres. Lengths of sarcomeres were determined using ImageJ (NIH, Public Domain) and subsequently converted to micrometers (91, 92).

RNA Extraction and Sequencing. Myocardial tissue of age- and gender-matched mice was obtained from the posterior wall of the LV. After a quick rinse in PBS to remove excess blood, the myocardial tissue was immediately snap-frozen. Homogenization of the LV myocardial tissue was done using 2.3-mm Zirconia/Silica beads, TRIzol reagent, and the Precellys bead beater system (Precellys24 Tissue homogenizer, Bertin Technologies). Total RNA was extracted using the TRIzol method (93) and subjected to Illumina TruSeq kit RNA V2 library generation and sequenced at a depth of 15–30 million single-end 50-base reads on an Illumina HiSEq. 2000. FASTQ files were aligned to the human genome build GRCh37 and University of California Santa Cruz transcriptome reference (94) using TopHat 2.0.9 (95) and Bowtie2 (96). Gene-level fragments per kilobase of transcript per million expression was also obtained with Cufflinks2 (97) (ccb.jhu.edu/software/tophat/igenomes.shtml).

Statistical Analysis. Statistical analysis was performed using GraphPad Prism v6. Echocardiographic and CMR data between experimental groups of mice were analyzed using nonparametric *t* tests or ANOVA. *P* values less than 0.05 were considered statistically significant. Values are expressed as mean ± SEM.

ACKNOWLEDGMENTS. We thank Anastacia Loberg, Katie Burke, and Devin Pillis for assistance with mouse procedures; Michelle Niemann for assistance with invasive hemodynamics; Dr. Uzmee Mendsaikhan for assistance with cardiac perfusions; Betsy DiPasquale for preparing histopathology slides; Victoria Moore and Christine Schulte for echocardiography; Scott Dunn for CMR; Dr. Diana Lindquist from the Imaging Research Core for her help with the CMR studies and specifically the phantom experiments; Chris Woods for technical support with image preparation; Dr. Tilat Rizvi for performing immunhistochemistry; and N.B.'s scientific oversight committee members, Drs. Carolyn Lutzko, Katherine Yutzey, and Theodosia Kalfa, for their time and input. This work was funded by the U01 HL117709 Excellence in Hemoglobinopathies Research Award (to P.M., J.A.T., and C.T.Q.), and the Arnold Strauss Fellowship Award (to N.B.).

1. Quinn CT, Rogers ZR, Buchanan GR (2004) Survival of children with sickle cell disease. *Blood* 103(11):4023–4027.
2. Lanzkron S, Carroll CP, Haywood C, Jr (2013) Mortality rates and age at death from sickle cell disease: U.S., 1979–2005. *Public Health Rep* 128(2):110–116.
3. Fitzhugh CD, et al. (2010) Cardiopulmonary complications leading to premature deaths in adult patients with sickle cell disease. *Am J Hematol* 85(1):36–40.
4. Darbari DS, et al. (2006) Circumstances of death in adult sickle cell disease patients. *Am J Hematol* 81(11):858–863.
5. Gladwin MT, et al. (2004) Pulmonary hypertension as a risk factor for death in patients with sickle cell disease. *N Engl J Med* 350(9):886–895.
6. James TN, Riddick L, Massing GK (1994) Sickle cells and sudden death: morphologic abnormalities of the cardiac conduction system. *J Lab Clin Med* 124(4):507–520.
7. Romero Mestre JC, Hernández A, Agramonte O, Hernández P (1997) Cardiovascular autonomic dysfunction in sickle cell anemia: A possible risk factor for sudden death? *Clin Auton Res* 7(3):121–125.
8. Fontaine JM, Ofili EO, Adenaike MB, VanDecker W, Haywood LJ (2008) Clinical assessment of the risk for sudden cardiac death in patients with sickle cell anemia. *J Natl Med Assoc* 100(4):360–368.
9. Hamideh D, Alvarez O (2013) Sickle cell disease related mortality in the United States (1999–2009). *Pediatr Blood Cancer* 60(9):1482–1486.
10. Baroldi G (1969) High resistance of the human myocardium to shock and red blood cell aggregation (sludge). *Cardiologia* 54(5):271–277.
11. Assanasen C, Quinton RA, Buchanan GR (2003) Acute myocardial infarction in sickle cell anemia. *J Pediatr Hematol Oncol* 25(12):978–981.
12. Chacko P, Kraut EH, Zweier J, Hitchcock C, Raman SV (2013) Myocardial infarction in sickle cell disease: Use of translational imaging to diagnose an under-recognized problem. *J Cardiovasc Transl Res* 6(5):752–761.
13. Wang H, Laslett LJ, Richman CM, Wun T (2004) Acute myocardial infarction in hemoglobin SC disease. *Ann Hematol* 83(10):622–624.
14. Martin CR, Johnson CS, Cobb C, Tatter D, Haywood LJ (1996) Myocardial infarction in sickle cell disease. *J Natl Med Assoc* 88(7):428–432.
15. Ataga KI, et al. (2006) Pulmonary hypertension in patients with sickle cell disease: A longitudinal study. *Br J Haematol* 134(1):109–115.
16. Voskaridou E, et al. (2007) Pulmonary hypertension in patients with sickle cell/beta thalassemia: Incidence and correlation with serum N-terminal pro-brain natriuretic peptide concentrations. *Haematologica* 92(6):738–743.
17. Gladwin MT, Vichinsky E (2008) Pulmonary complications of sickle cell disease. *N Engl J Med* 359(21):2254–2265.
18. Parent F, et al. (2011) A hemodynamic study of pulmonary hypertension in sickle cell disease. *N Engl J Med* 365(1):44–53.
19. De Castro LM, Jonassaint JC, Graham FL, Ashley-Koch A, Telen MJ (2008) Pulmonary hypertension associated with sickle cell disease: Clinical and laboratory endpoints and disease outcomes. *Am J Hematol* 83(1):19–25.
20. Hebbel RP (2011) Reconstructing sickle cell disease: A data-based analysis of the "hyperhemolysis paradigm" for pulmonary hypertension from the perspective of evidence-based medicine. *Am J Hematol* 86(2):123–154.
21. Reiter CD, et al. (2002) Cell-free hemoglobin limits nitric oxide bioavailability in sickle-cell disease. *Nat Med* 8(12):1383–1389.
22. Morris CR, et al. (2005) Dysregulated arginine metabolism, hemolysis-associated pulmonary hypertension, and mortality in sickle cell disease. *JAMA* 294(1):81–90.
23. Reiter CD, Gladwin MT (2003) An emerging role for nitric oxide in sickle cell disease vascular homeostasis and therapy. *Curr Opin Hematol* 10(2):99–107.
24. Sachdev V, et al.; Walk-PHASST Investigators (2011) Echocardiographic markers of elevated pulmonary pressure and left ventricular diastolic dysfunction are associated with exercise intolerance in adults and adolescents with homozygous sickle cell anemia in the United States and United Kingdom. *Circulation* 124(13):1452–1460.
25. Caughey MC, Hinderliter AL, Jones SK, Shah SP, Ataga KI (2012) Hemodynamic characteristics and predictors of pulmonary hypertension in patients with sickle cell disease. *Am J Cardiol* 109(9):1353–1357.
26. Castro O, Hoque M, Brown BD (2003) Pulmonary hypertension in sickle cell disease: Cardiac catheterization results and survival. *Blood* 101(4):1257–1261.
27. Kasner M, et al. (2007) Utility of Doppler echocardiography and tissue Doppler imaging in the estimation of diastolic function in heart failure with normal ejection fraction: A comparative Doppler-conductance catheterization study. *Circulation* 116(6):637–647.
28. Mehari A, Gladwin MT, Tian X, Machado RF, Kato GJ (2012) Mortality in adults with sickle cell disease and pulmonary hypertension. *JAMA* 307(12):1254–1256.
29. Fonseca GH, Souza R, Salemi VM, Jardim CV, Gualandro SF (2012) Pulmonary hypertension diagnosed by right heart catheterisation in sickle cell disease. *Eur Respir J* 39(1):112–118.
30. Sutton LL, Castro O, Cross DJ, Spencer JE, Lewis JF (1994) Pulmonary hypertension in sickle cell disease. *Am J Cardiol* 74(6):626–628.
31. Covitz W, et al.; The Cooperative Study of Sickle Cell Disease (CSSCD) (1995) The heart in sickle cell anemia. *Chest* 108(5):1214–1219.
32. Lindsay J, Jr, Meshel JC, Patterson RH (1974) The cardiovascular manifestations of sickle cell disease. *Arch Intern Med* 133(4):643–651.
33. Lester LA, Sodt PC, Hutcheon N, Arcilla RA (1990) Cardiac abnormalities in children with sickle cell anemia. *Chest* 98(5):1169–1174.
34. Covarrubias EA, Sheikh MU, Solanki DL, Morjaria M, Fox LM (1980) Left ventricular function in sickle cell anemia: A noninvasive evaluation. *South Med J* 73(3):342–344.
35. Gerry JL, Baird MG, Fortuin NJ (1976) Evaluation of left ventricular function in patients with sickle cell anemia. *Am J Med* 60(7):968–972.
36. Doshi AR, Pauliks LB (2013) Increased left main coronary artery dimensions in children with sickle cell disease. *Pediatr Cardiol* 34(4):954–958.
37. Sachdev V, et al. (2007) Diastolic dysfunction is an independent risk factor for death in patients with sickle cell disease. *J Am Coll Cardiol* 49(4):472–479.
38. Johnson MC, et al. (2010) Left ventricular hypertrophy and diastolic dysfunction in children with sickle cell disease are related to asleep and waking oxygen desaturation. *Blood* 116(1):16–21.
39. Arslankoylu AE, Hallioglu O, Yilgor E, Duzovali O (2010) Assessment of cardiac functions in sickle cell anemia with Doppler myocardial performance index. *J Trop Pediatr* 56(3):195–197.

40. Cabrita IZ, et al. (2013) The association between tricuspid regurgitation velocity and 5-year survival in a North West London population of patients with sickle cell disease in the United Kingdom. *Br J Haematol* 162(3):400–408.
41. Isma'eel H, et al. (2008) Relation between iron-overload indices, cardiac echo-Doppler, and biochemical markers in thalassemia intermedia. *Am J Cardiol* 102(3):363–367.
42. Junqueira FP, et al. (2013) Right and left ventricular function and myocardial scarring in adult patients with sickle cell disease: a comprehensive magnetic resonance assessment of hepatic and myocardial iron overload. *J Cardiovasc Magn Reson* 15:83.
43. Hankins JS, et al. (2010) Ventricular diastolic dysfunction in sickle cell anemia is common but not associated with myocardial iron deposition. *Pediatr Blood Cancer* 55(3):495–500.
44. Voskaridou E, Christoulas D, Terpos E (2012) Sickle-cell disease and the heart: Review of the current literature. *Br J Haematol* 157(6):664–673.
45. Ataga KI, Klings ES (2014) Pulmonary hypertension in sickle cell disease: Diagnosis and management. *Hematology (Am Soc Hematol Educ Program)* 2014(1):425–431.
46. Klings ES, et al.; American Thoracic Society Ad Hoc Committee on Pulmonary Hypertension of Sickle Cell Disease (2014) An official American Thoracic Society clinical practice guideline: Diagnosis, risk stratification, and management of pulmonary hypertension of sickle cell disease. *Am J Respir Crit Care Med* 189(6):727–740.
47. Westwood MA, et al. (2007) Myocardial tissue characterization and the role of chronic anemia in sickle cell cardiomyopathy. *J Magn Reson Imaging* 26(3):564–568.
48. Bratis K, et al. (2013) Abnormal myocardial perfusion-fibrosis pattern in sickle cell disease assessed by cardiac magnetic resonance imaging. *Int J Cardiol* 166(3):e75–e76.
49. Pászty C, et al. (1997) Transgenic knockout mice with exclusively human sickle hemoglobin and sickle cell disease. *Science* 278(5339):876–878.
50. Eddine AC, et al. (2012) Ventricular structure and function in children with sickle cell disease using conventional and tissue Doppler echocardiography. *Am J Cardiol* 109(9): 1358–1364.
51. Zilberman MV, Du W, Das S, Sarnaik SA (2007) Evaluation of left ventricular diastolic function in pediatric sickle cell disease patients. *Am J Hematol* 82(6):433–438.
52. Arheden H, et al. (1999) Measurement of the distribution volume of gadopentetate dimeglumine at echo-planar MR imaging to quantify myocardial infarction: Comparison with 99mTc-DTPA autoradiography in rats. *Radiology* 211(3):698–708.
53. Flett AS, et al. (2010) Equilibrium contrast cardiovascular magnetic resonance for the measurement of diffuse myocardial fibrosis: Preliminary validation in humans. *Circulation* 122(2):138–144.
54. Neilan TG, et al. (2013) Myocardial extracellular volume fraction from T1 measurements in healthy volunteers and mice: Relationship to aging and cardiac dimensions. *JACC Cardiovasc Imaging* 6(6):672–683.
55. Rodgers CT, et al. (2013) Inversion recovery at 7 T in the human myocardium: Measurement of T(1), inversion efficiency and B(1) (+). *Magn Reson Med* 70(4):1038–1046.
56. Arumugam PI, et al. (2015) Genetic diminution of circulating prothrombin ameliorates multiorgan pathologies in sickle cell disease mice. *Blood* 126(15):1844–1855.
57. Tomanek RJ, Grimes JC, Diana JN (1981) Relationship between the magnitude of myocardial ischemia and ultrastructural alterations. *Exp Mol Pathol* 35(1):65–83.
58. Vandeplassche G, Thoné F, Hermans C, Borgers M (1990) Ultrastructural damage and Ca2(+)-shifts in the canine myocardium subjected to regional incomplete ischemia. *Basic Res Cardiol* 85(4):384–391.
59. Tanne Z, et al. (1994) Ultrastructural and cytochemical changes in the heart of iron-deficient rats. *Biochem Pharmacol* 47(10):1759–1766.
60. Dong F, et al. (2005) Dietary iron deficiency induces ventricular dilation, mitochondrial ultrastructural aberrations and cytochrome c release: Involvement of nitric oxide synthase and protein tyrosine nitration. *Clin Sci (Lond)* 109(3):277–286.
61. Asrar Ul Haq M, Mutha V, Rudd N, Hare DL, Wong C (2014) Heart failure with preserved ejection fraction—Unwinding the diagnosis mystique. *Am J Cardiovasc Dis* 4(3):100–113.
62. Pape LA, Price JM, Alpert JS, Ockene IS, Weiner BH (1991) Relation of left atrial size to pulmonary capillary wedge pressure in severe mitral regurgitation. *Cardiology* 78(4):297–303.
63. Patel DA, Lavie CJ, Milani RV, Shah S, Gilliland Y (2009) Clinical implications of left atrial enlargement: A review. *Ochsner J* 9(4):191–196.
64. Appleton CP, Galloway JM, Gonzalez MS, Gaballa M, Basnight MA (1993) Estimation of left ventricular filling pressures using two-dimensional and Doppler echocardiography in adult patients with cardiac disease. Additional value of analyzing left atrial size, left atrial ejection fraction and the difference in duration of pulmonary venous and mitral flow velocity at atrial contraction. *J Am Coll Cardiol* 22(7):1972–1982.
65. Machado RF, et al. (2007) Severity of pulmonary hypertension during vaso-occlusive pain crisis and exercise in patients with sickle cell disease. *Br J Haematol* 136(2):319–325.
66. Anthi A, et al. (2007) Hemodynamic and functional assessment of patients with sickle cell disease and pulmonary hypertension. *Am J Respir Crit Care Med* 175(12): 1272–1279.
67. Denfield SW, Webber SA (2010) Restrictive cardiomyopathy in childhood. *Heart Fail Clin* 6(4):445–452, viii.
68. Russo LM, Webber SA (2005) Idiopathic restrictive cardiomyopathy in children. *Heart* 91(9):1199–1202.
69. Webber SA, et al.; Pediatric Cardiomyopathy Registry Investigators (2012) Outcomes of restrictive cardiomyopathy in childhood and the influence of phenotype: A report from the Pediatric Cardiomyopathy Registry. *Circulation* 126(10):1237–1244.
70. Foley RN, et al. (1996) The impact of anemia on cardiomyopathy, morbidity, and mortality in end-stage renal disease. *Am J Kidney Dis* 28(1):53–61.
71. Metivier F, Marchais SJ, Guerin AP, Pannier B, London GM (2000) Pathophysiology of anaemia: Focus on the heart and blood vessels. *Nephrol Dial Transplant* 15(Suppl 3): 14–18.
72. Srivastava PM, et al. (2006) Diastolic dysfunction is associated with anaemia in patients with type II diabetes. *Clin Sci (Lond)* 110(1):109–116.
73. Nair D, et al. (2005) Association of anemia with diastolic dysfunction among patients with coronary artery disease in the Heart and Soul Study. *Am J Cardiol* 95(3):332–336.
74. Cho IJ, Mun YC, Kwon KH, Shin GJ (2014) Effect of anemia correction on left ventricular structure and filling pressure in anemic patients without overt heart disease. *Korean J Intern Med* 29(4):445–453.
75. Rakusan K, Cicutti N, Kolar F (2001) Effect of anemia on cardiac function, microvascular structure, and capillary hematocrit in rat hearts. *Am J Physiol Heart Circ Physiol* 280(3):H1407–H1414.
76. Rossi MA, Carillo SV (1983) Electron microscopic study on the cardiac hypertrophy induced by iron deficiency anaemia in the rat. *Br J Exp Pathol* 64(4):373–387.
77. Desai AA, et al. (2014) Mechanistic insights and characterization of sickle cell disease-associated cardiomyopathy. *Circ Cardiovasc Imaging* 7(3):430–437.
78. Fertrin KY, Costa FF (2010) Genomic polymorphisms in sickle cell disease: Implications for clinical diversity and treatment. *Expert Rev Hematol* 3(4):443–458.
79. Chang KH, et al. (2015) Vasculopathy-associated hyperangiotensinemia mobilizes haematopoietic stem cells/progenitors through endothelial AT_2R and cytoskeletal dysregulation. *Nat Commun* 6:5914.
80. Sawicki KT, et al. (2015) Increased heme levels in the heart lead to exacerbated ischemic injury. *J Am Heart Assoc* 4(8):e002272.
81. Khechaduri A, Bayeva M, Chang HC, Ardehali H (2013) Heme levels are increased in human failing hearts. *J Am Coll Cardiol* 61(18):1884–1893.
82. Acehan D, et al. (2011) Cardiac and skeletal muscle defects in a mouse model of human Barth syndrome. *J Biol Chem* 286(2):899–908.
83. Heiberg E, et al. (2010) Design and validation of Segment—Freely available software for cardiovascular image analysis. *BMC Med Imaging* 10:1.
84. Wansapura JP, Millay DP, Dunn RS, Molkentin JD, Benson DW (2011) Magnetic resonance imaging assessment of cardiac dysfunction in δ-sarcoglycan null mice. *Neuromuscul Disord* 21(1):68–73.
85. Messroghli DR, et al. (2011) Assessment of diffuse myocardial fibrosis in rats using small-animal Look-Locker inversion recovery T1 mapping. *Circ Cardiovasc Imaging* 4(6):636–640.
86. Abeykoon S, Sargent M, Wansapura JP (2012) Quantitative myocardial perfusion in mice based on the signal intensity of flow sensitized CMR. *J Cardiovasc Magn Reson* 14:73.
87. Chu V, et al. (2001) Method for non-invasively recording electrocardiograms in conscious mice. *BMC Physiol* 1:6.
88. Desai KH, et al. (1997) Cardiovascular indexes in the mouse at rest and with exercise: New tools to study models of cardiac disease. *Am J Physiol* 272(2 Pt 2):H1053–H1061.
89. Parsons SA, et al. (2007) Genetic disruption of calcineurin improves skeletal muscle pathology and cardiac disease in a mouse model of limb-girdle muscular dystrophy. *J Biol Chem* 282(13):10068–10078.
90. Woessner JF, Jr (1961) The determination of hydroxyproline in tissue and protein samples containing small proportions of this imino acid. *Arch Biochem Biophys* 93: 440–447.
91. Maiellaro-Rafferty K, et al. (2013) Altered regional cardiac wall mechanics are associated with differential cardiomyocyte calcium handling due to nebulette mutations in preclinical inherited dilated cardiomyopathy. *J Mol Cell Cardiol* 60:151–160.
92. Gupta MK, et al. (2013) Functional dissection of myosin binding protein C phosphorylation. *J Mol Cell Cardiol* 64:39–50.
93. Brattelid T, et al. (2007) Expression of mRNA encoding G protein-coupled receptors involved in congestive heart failure—A quantitative RT-PCR study and the question of normalisation. *Basic Res Cardiol* 102(3):198–208.
94. Karolchik D, et al. (2014) The UCSC Genome Browser database: 2014 update. *Nucleic Acids Res* 42(Database issue, D1):D764–D770.
95. Kim D, et al. (2013) TopHat2: Accurate alignment of transcriptomes in the presence of insertions, deletions and gene fusions. *Genome Biol* 14(4):R36.
96. Langmead B, Trapnell C, Pop M, Salzberg SL (2009) Ultrafast and memory-efficient alignment of short DNA sequences to the human genome. *Genome Biol* 10(3):R25.
97. Trapnell C, et al. (2012) Differential gene and transcript expression analysis of RNA-seq experiments with TopHat and Cufflinks. *Nat Protoc* 7(3):562–578.